

# **Ni-N<sub>x</sub> Single Sites Embedded in Multilayer Graphene Generated from Nitrogen-Rich Metal-organic Framework for Highly Selective Electrocatalytic CO<sub>2</sub> Reduction**

Haojing Wang,<sup>a</sup> Wenguang Tu,<sup>a</sup> Yan Lu,<sup>a,b</sup> Guanyu Liu,<sup>a,b</sup> Shuyang Wu,<sup>a,b</sup> Chunping Chen,<sup>c</sup>

Dermot O'Hare<sup>c</sup> and Rong Xu<sup>a,b,\*</sup>

<sup>a</sup>School of Chemical & Biomedical Engineering, Nanyang Technological University, 62 Nanyang Drive, Singapore 637459, Singapore

<sup>b</sup>Cambridge Centre for Advanced Research and Education in Singapore (CARES), CREATE Tower, 1 Create Way, Singapore 138602, Singapore

<sup>c</sup>Chemistry Research Laboratory, Department of Chemistry, University of Oxford, 12 Mansfield Road, Oxford OX1 3TA, United Kingdom

\*E-mail: [rxu@ntu.edu.sg](mailto:rxu@ntu.edu.sg)

## Abstract

CO<sub>2</sub> electroreduction has been regarded as a feasible pathway for CO<sub>2</sub> utilization when the cost of renewable electricity can be substantially reduced in future. Development of highly active and selective catalysts for CO<sub>2</sub> reduction still poses significant challenges. In this work, we report the use of ligand environment of metal-organic frameworks (MOFs) to influence the formation of M-N-C active site. The use of amine-containing ligand, 2-amino-1,4-benzenedicarboxylic acid, in the Ni-based MOF precursor in combination with appropriate annealing temperature and mild post-treatment leads to the catalyst containing Ni-N<sub>x</sub> single sites embedded in multilayer nitrogen-doped graphene. The as-prepared catalyst displays excellent electrochemical CO<sub>2</sub> reduction to CO with Faradaic efficiencies (FE) above 90% in a wide range of potentials from -0.6 to -1.2 V (vs. RHE). A maximum FE of 97% can be obtained at a low overpotential of 0.79 V with a remarkable CO partial current density (27.2 mA cm<sup>-2</sup>), which is among the best performances of Ni-based catalysts reported so far. Control study using 1,4-benzenedicarboxylic acid as the ligand indicated C-N and Ni-N bonds in amine-containing MOF affect the property both Ni and graphene in a synergistic way, resulting in the formation of highly efficient Ni-N<sub>x</sub> single sites for CO<sub>2</sub> reduction to CO. This work has provided new insights into tuning the chemical environment of MOF precursors towards developing better electrocatalysts after annealing and post-treatment.

## Keywords:

Electrocatalysis, CO<sub>2</sub> reduction, metal-organic framework, graphene, single sites

## 1. Introduction

Carbon dioxide, CO<sub>2</sub>, is an extremely stable gas in the atmosphere from the thermodynamic perspective [1]. However, the worldwide greenhouse effect caused by excessive accumulating CO<sub>2</sub> emission from combustion of fossil fuels and other anthropogenic activities, has aroused extensive concerns in recent decades [2, 3].

Electrochemical CO<sub>2</sub> reduction using renewable electricity has been regarded as one of most attractive ways to convert CO<sub>2</sub> to C<sub>1</sub> feedstock such as carbon monoxide (CO) and formic acid, or other value-added chemicals after further processing [4-6]. Although great advances in this field have been achieved over the past years, its widespread application at an industrial scale is still being challenged due to: (1) excessive overpotential (or low energetic efficiency), (2) large kinetic barrier for the first electron transfer to the adsorbed CO<sub>2</sub> molecule, and (3) poor selectivity for desired products [7, 8]. Additionally, hydrogen evolution reaction (HER) is a competitive two-electron transfer process occurring at a wide range of potentials, which makes CO<sub>2</sub> reduction more challenging. Therefore, continuously seeking for new catalysts and modification of existing electrocatalysts are necessary to overcome these limitations [9, 10].

The process of CO<sub>2</sub> reduction to CO ( $\text{CO}_2 + 2\text{H}^+ + 2\text{e}^- \rightarrow \text{CO} + \text{H}_2\text{O}$ , -0.11 V vs. reversible hydrogen electrode, RHE) is a relatively facile pathway with two electrons transfer compared with other multiple electron/proton-transfer pathways [11]. Au, Ag, Pd, Pd-Au and Au-Cu catalysts have been demonstrated with excellent CO<sub>2</sub> reduction selectivity for CO by numerous previous studies [12-20]. However, the high cost and scarce reserves of these noble metals will limit the practical application in a large scale [21, 22]. Thanks to their intrinsic activities and earth-abundant nature, transition metals like Fe, Co, Ni and Cu-based materials are proved as possible alternatives to noble metal catalysts [23-26]. Among them, Cu-based catalysts are more prone to catalyze CO<sub>2</sub> reduction to a wide range of hydrocarbons [27]. In recent years, single-atom catalysts (SACs) have attracted great attention for CO oxidation, oxygen reduction, and CO<sub>2</sub> reduction, due to their remarkable activity and high stability [28-35]. Despite these progresses achieved over SACs, there is still considerable difficulty in dispersing metal single atoms on carbon supports. Physical techniques, such as atomic layer deposition, mass-selected molecules or atom beams are required to precisely regulate the surface structure of the support, leading to high cost and low yield of single atoms. Furthermore, SACs without strong interaction with the support can easily aggregate during the post-treatment or reactions. In order to maximize turnover frequency (TOF) of the catalysts,

new synthetic approaches need to be developed to obtain small nanoclusters or SACs for efficient and selective CO<sub>2</sub> reduction [36]. The atomic transition metal coordinated with those nitrogen doped in carbon materials could generate M-N-C (M=Mn, Fe, Co, Ni, Cu) catalysts. N-doped porous carbon nanomaterials have been found to be ideal support materials for transition metal single atoms with more efficient charge-transfer and stronger chemical bonds between low-coordination metal single atoms and electronegative N atoms [37]. Within M-N-C catalysts, M-N<sub>x</sub> moieties work as efficient active sites for CO<sub>2</sub> reduction [38-42]. Especially, Ni-N<sub>x</sub> moiety has been demonstrated with efficient electrocatalytic performance for CO<sub>2</sub> reduction to CO with suppressed HER activity [43-45]. Möller et al. obtained Ni-N<sub>x</sub> motifs of solid Ni-N-C catalysts which displays stable FE of CO<sub>2</sub> reduction to CO around 85% with considerable CO partial current density above 200 mA cm<sup>-2</sup> for 20 h on a gas diffusion electrode [46]. Zhang et al. reported Ni-N moieties as the active component in Ni/NC catalysts synthesized by utilizing polyacrylonitrile as the nitrogen source and achieved CO<sub>2</sub>-to-CO conversion with high FEs (≥84.7%) in a wide potential range from -0.8 to -1.2 V (vs. RHE)[47]. Recently, our group successfully anchored isolated Ni atoms in the nitrogen-doped ultrathin porous carbon nanosheet and realized a FE of 96% with high current density of 26.4 mA cm<sup>-2</sup> to convert CO<sub>2</sub> to CO via a polydopamine-assisted g-C<sub>3</sub>N<sub>4</sub> template method[35]. With heteroatom-containing organic ligands and metal ions, metal-organic frameworks (MOFs) can serve as ideal precursors to feasibly afford SACs with interactions between N/O/S and metal atoms for electrochemical application by high-temperature pyrolysis [48]. Although some MOF-derived M-N-C materials have been reported for electrocatalytic CO<sub>2</sub> reduction in past few years, most of them were derived from limited types of MOFs, such as ZIF-8 and ZIF-67 with insufficient understanding about the effect of MOF precursors on the property and performance of the final catalysts generated.

Herein, we report a strategy to synthesize active Ni-N<sub>x</sub> single sites embedded in multilayer nitrogen-doped graphene (denoted as Ni-NG-acid) by high-temperature annealing of a specific NH<sub>2</sub>-containing MOF precursor and subsequent acid treatment. The catalyst was demonstrated to exhibited efficient electrocatalytic activity with over



90% selectivity for CO<sub>2</sub> to CO in a wide range of potential and achieves the maximal FE<sub>CO</sub> of 97% at a low overpotential of 0.79 V with a superior CO partial current density of 27.2 mA cm<sup>-2</sup>. From a point of view on atomic level, it was found from this work that the NH<sub>2</sub>-containing ligand in MOF precursors could facilitate the formation of Ni-N<sub>x</sub> active sites not only by generating new Ni-N coordination environment with extra nitrogen source from amine group but also by leading to abundant defects and C-N cleavage on graphene shells after annealing, which could result in further aggregation of Ni nanoparticles (Ni NPs). The property of multilayer graphene and aggregation of Ni particles can also be governed by tuning the annealing temperature to derive optimal annealing condition for desired Ni-N-C catalyst.

## **2. Experimental section**

### **2.1 Materials**

Nickel (II) nitrate hexahydrate (Ni(NO<sub>3</sub>)<sub>2</sub>·6H<sub>2</sub>O, Sigma-Aldrich), 2-amino-1,4-benzenedicarboxylic acid (NH<sub>2</sub>-BDC, Aldrich), 1,4-benzenedicarboxylic acid (BDC, Aldrich), triethylenediamine (TED, Sigma-Aldrich), N,N-Dimethylmethanamide (DMF, Sigma-Aldrich, ACS reagent), Ethanol (C<sub>2</sub>H<sub>5</sub>OH, Sinopharm Chemical Reagent), sulfuric acid (H<sub>2</sub>SO<sub>4</sub>, Sigma-Aldrich), potassium bicarbonate (KHCO<sub>3</sub>, Sigma-Aldrich, ACS reagent), nickel (II) phthalocyanine (C<sub>32</sub>H<sub>16</sub>N<sub>8</sub>Ni, Alfa Aesar), Nafion® perfluorinated resin solution (Aldrich, 5 wt.% in lower aliphatic alcohols and water, contains 15-20% water).

### **2.2 Material synthesis**

#### **2.2.1 Preparation of NH<sub>2</sub>-Ni-MOF and Ni-MOF**

Typically, Ni(NO<sub>3</sub>)<sub>2</sub>·6H<sub>2</sub>O (0.6 g, 2 mmol), NH<sub>2</sub>-BDC (0.37 g, 2 mmol) and TED (0.12 g, 1 mmol) were dissolved in DMF (50 mL) and sonicated for 5 mins. The solution was then heated at 130 °C in an oil bath with stirring for 24 h. After reaction, the mixture was cooled down to room temperature. The precipitates were collected by centrifugation, then washed by DMF and ethanol for several times. The sample was finally dried in a vacuum oven at 60 °C overnight to derive NH<sub>2</sub>-Ni-MOF. The synthesis

procedure of Ni-MOF is the same with NH<sub>2</sub>-Ni-MOF but only replacing NH<sub>2</sub>-BDC by BDC (2 mmol).

### **2.2.2 Preparation of Ni-NG and Ni-NG-acid**

The as-synthesized NH<sub>2</sub>-Ni-MOF were put into the tubular furnace for annealing at 1000 °C for 2 h under a N<sub>2</sub> flow with a heating rate of 2 °C min<sup>-1</sup> to derive Ni-NG. Then the as-synthesized Ni-NG was further treated with 0.5 M H<sub>2</sub>SO<sub>4</sub> at 80 °C for 6 h. The final product was then washed with a large amount of distilled water (to reach pH = 7) and lyophilized to derive Ni-NG-acid.

### **2.2.3 Preparation of Ni-NG-X-acid**

The synthesis and acid treatment procedure of Ni-NG-X-acid is the same with Ni-NG-acid but only varying the annealing temperature to X (X=700, 800, 900, 1100 °C).

### **2.2.4 Preparation of Ni-NG-2M acid**

The as-synthesized Ni-NG was further treated with 2 M H<sub>2</sub>SO<sub>4</sub> at 80 °C for 6 h. The final product was then washed with a large amount of distilled water (to reach pH = 7) and lyophilized to derive Ni-NG-2M acid.

### **2.2.5 Preparation of Ni-NG-val acid**

The as-synthesized Ni-NG was further sonicated in 37 wt.% HCl for 4 h followed by repeating distilled water wash and centrifugation (to reach pH = 7). Then ball milling process was performed to the catalyst for 1 h. After the ball milling, the powder was further sonicated in 37 wt.% HCl for 12 h. After washed by a large amount of distilled water to reach pH = 7, the final product was finally collected by centrifugation and lyophilization to derive Ni-NG-val acid.

### **2.2.6 Preparation of Ni NPs@NG and Ni NPs@NG-acid**

The as-synthesized Ni-MOF were put into the tubular furnace for annealing at 1000 °C for 2 h under a N<sub>2</sub> flow with a heating rate of 2 °C min<sup>-1</sup> to derive Ni NPs@NG. Then the product was further treated with 0.5 M H<sub>2</sub>SO<sub>4</sub> at 80 °C for 6 h. The final product was then washed with a large amount of distilled water (to reach pH = 7) and lyophilized to derive Ni NPs@NG-acid.

## **2.3 Characterization**

XRD was performed on Bruker D2 Phaser X-ray diffractometer. ATR-FTIR spectroscopy was derived from Thermo Scientific Nicolet iS50 FTIR Spectrometer. SEM images were taken from JEOL JSM-6701F SEM, TEM images were taken from JEM 2100PLUS TEM, HAADF-STEM images were taken from JEOL ARM 200F. XPS analysis was conducted on Kratos Axis Ultra spectrometer using Al K $\alpha$  radiation and the C 1s peak at 284.8 eV as internal standard. Raman spectra were obtained in Renishaw InVia Reflex Raman with a 514 nm excitation wavelength. The samples were degassed at 300 °C for 24 h and the obtained adsorption-desorption isotherms were recorded to give the BET specific area on Micromeritics-3Flex. ICP-OES measurements were conducted on PerkinElmer Optima 8000. The carbon and nitrogen contents in samples were measured by Elementar Vario EL III Elemental Analyzer. The contact angle was measured by KRUSS DSA25 Contact Angle Analyzer. The liquid product was analyzed by Bruker Avance II 300MHz NMR Spectrometer, where 0.5 mL electrolyte collected after electrochemical test was mixed with 0.1 mL deuterated water (D<sub>2</sub>O) and 0.5  $\mu$ L dimethyl sulfoxide (DMSO). The gas product analysis for the electrochemical experiments was carried out using Agilent 7890A gas chromatograph (GC) system.

## 2.4 Electrochemical measurements

The electrochemical experiments were conducted in a gas-tight H-type cell with two compartments separated by a Nafion® 117 proton exchange membrane. The Pt plate and Ag/AgCl reference electrode (saturated KCl) was used as the counter electrode and reference electrode. The working electrode was prepared by the following procedure: 4 mg of the catalyst was dispersed into 960  $\mu$ L of ethanol with 40  $\mu$ L of Nafion solution (Sigma Aldrich, 5 wt%) and then 80  $\mu$ L of the catalyst ink was loaded onto one end of a carbon fiber paper (Toray Paper 060) with  $0.6 \times 1 \text{ cm}^2$  (the carbon paper was cut as  $0.6 \times 2 \text{ cm}^2$ ) after 40-min ultrasonication. 60 mL 0.5 M KHCO<sub>3</sub> was added into each compartment as electrolyte and the electrolyte in the cathodic compartment was stirred at 600 rpm. The linear sweep voltammetry (LSV) and electrolysis measurement at controlled potentials were performed in Ar- or CO<sub>2</sub>-saturated 0.5 M KHCO<sub>3</sub> solution

with a scan rate of 10 mV s<sup>-1</sup>. The potentials were controlled by an electrochemical working station CHI 660E (CH Instruments Ins., Shanghai, China). All potentials in this study were reported with the conversion  $E \text{ (vs. RHE)} = E \text{ (vs. Ag/AgCl)} + 0.197 + 0.059 \times \text{pH}$ . CO<sub>2</sub> (or Ar) gas was delivered at an average rate of 10 mL min<sup>-1</sup> to the GC system and went through a gas sampling loop (0.25 mL). The gas phase composition was analyzed by GC every 20 min (including post run). Among the gas products, H<sub>2</sub> was analyzed by a thermal conductivity detector (TCD) and CO was analyzed by a flame ionization detector (FID). Electrolyte in cathodic compartment was collected after electrochemical measurement for liquid products analysis.

The FE<sub>CO</sub> at certain potential was calculated by the following equation:

$$\text{FE}_{\text{CO}} = \frac{Q_{\text{CO}}}{Q_{\text{Total}}} \times 100\% = \frac{\alpha n F}{Q_{\text{Total}}} \times 100\%$$

Where  $Q_{\text{CO}}$  is the number of electrons for CO production passed the electrode during the electrolysis,  $Q_{\text{Total}}$  is total number of electrons passed the electrons during the electrolysis,  $\alpha$  is the number of electrons transferred from CO<sub>2</sub> to CO ( $\alpha = 2$ ),  $n$  is the number of moles for CO production,  $F$  is the Faraday's constant ( $F = 96458 \text{ C mol}^{-1}$ ).

The TOF for CO production was calculated on the basis of total Ni content by the following equation:

$$\text{TOF} = \frac{I_{\text{CO}}/\alpha F}{m_{\text{cat}}x/M_{\text{Ni}}}$$

Where  $I_{\text{CO}}$  is the partial current of CO,  $\alpha$  is the number of electrons transferred from CO<sub>2</sub> to CO ( $\alpha = 2$ ),  $F$  is the Faraday's constant ( $F = 96458 \text{ C mol}^{-1}$ ),  $m_{\text{cat}}$  is the mass of catalyst loaded onto carbon paper electrode,  $x$  is the weight percentage of Ni in catalysts,  $M_{\text{Ni}}$  is the atomic mass of Ni ( $M_{\text{Ni}} = 58.69 \text{ g mol}^{-1}$ ).

### 3. Results and discussion

As illustrated in Fig. 1, the preparation of the catalyst was started with the synthesis of a Ni-based MOF, Ni<sub>2</sub>(NH<sub>2</sub>-BDC)<sub>2</sub>(TED) (denoted as NH<sub>2</sub>-Ni-MOF) as the precursor (see the experimental section). A camel-colored precipitate (Fig. S1a) was obtained. For comparison, another Ni-based MOF Ni<sub>2</sub>(BDC)<sub>2</sub>TED (denoted as Ni-MOF) with green color (Fig. S1b) was synthesized by the same method but replacing the NH<sub>2</sub>-BDC

ligands by 1,4-benzenedicarboxylic acid (BDC) according to our previous work [49]. The scanning electron microscopy (SEM) images (Fig. S2) show the nanoflake and nanosheet-like morphology of  $\text{NH}_2\text{-Ni-MOF}$  and  $\text{Ni-MOF}$ , respectively.

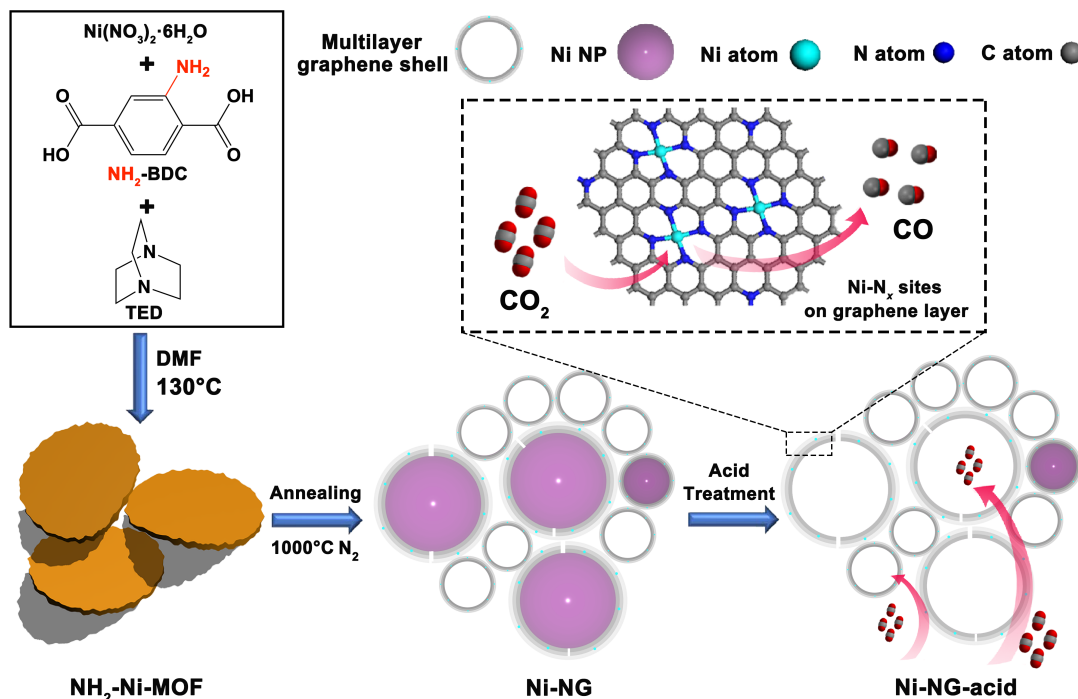


**Fig. 1.** Schematic illustration of the preparation process of Ni-NG-acid.

The powder X-ray diffraction (XRD) patterns indicate that these two MOFs were successfully synthesized and have different crystal structures (Fig. S3). As single crystals were not obtained in this study, FTIR analysis was attempted to reveal the structural information of the MOFs synthesized. The ATR-FTIR spectra of both MOFs and their corresponding BDC and  $\text{NH}_2\text{-BDC}$  ligands are shown in Fig. 2. It is noticed that one of two peaks at  $3504$  and  $3386\text{ cm}^{-1}$  which are attributed to asymmetric and symmetric N-H stretching of  $\text{-NH}_2$  in  $\text{NH}_2\text{-BDC}$  ligand is absent in  $\text{NH}_2\text{-Ni-MOF}$  [50, 51]. Instead, the latter displays only a red-shifted peak at  $3300\text{ cm}^{-1}$ , indicating  $\text{Ni}^{2+}$  is coordinated with the amine group [52]. An additional weak peak at  $3133\text{ cm}^{-1}$  is probably the overtone of C-N-H stretch/bend near  $1540\text{ cm}^{-1}$  [53]. Although it is difficult to reveal the structure of the MOFs at this stage, it is clear that the  $\text{-NH}_2$  functional group in the linker besides the carbonate group is also coordinated with the metal cation. The different coordination environment in  $\text{NH}_2\text{-Ni-MOF}$  compared to that

in Ni-MOF should lead to different properties of Ni catalyst after high temperature annealing.

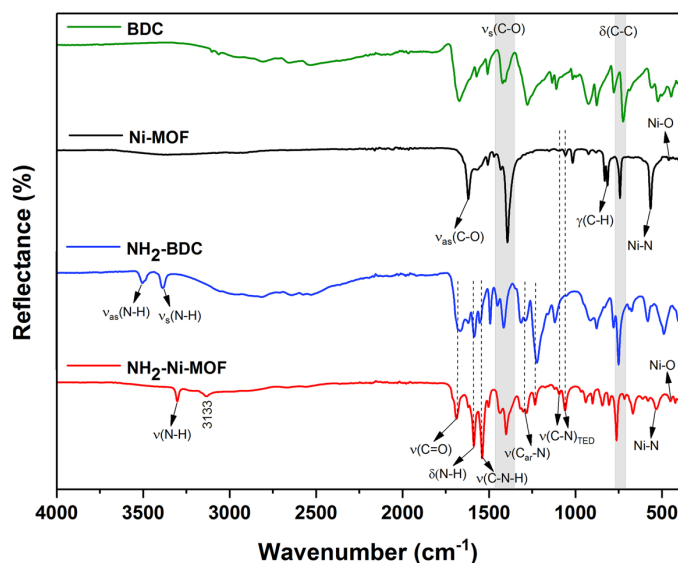


**Fig. 2.** ATR-FTIR spectra of BDC ligand, Ni-MOF, NH<sub>2</sub>-BDC ligand and NH<sub>2</sub>-Ni-MOF.

Upon annealing at 1000 °C under nitrogen atmosphere, black powders (denoted as Ni-NG) were obtained from NH<sub>2</sub>-Ni-MOF. The representative SEM (Fig. S4) images of Ni-NG show that the material maintains the same nanoflake structure with a large amount of sphere-like nanostructures. The TEM images further displays that some large particles with the size of 50-200 nm are coated by graphene shell with an interlayer distance of 0.34 nm in Fig S5a,b. The hollow shell structures and few metallic core encapsulated in graphene layers are also observed (Fig. S5c,d). After acid treatment in 0.5 M H<sub>2</sub>SO<sub>4</sub> (denoted as Ni-NG-acid), the nanoflake morphology of Ni-NG-acid is proved by SEM without any change (in Fig. S6). TEM images in Fig. 3a show that the larger Ni particles have been completely removed and most of the smaller nanoparticles are leached out as well, leaving behind densely packed hollow graphene shells with the size of 10-15 nm (Fig. 3b,c). Correspondingly, the percentage of Ni is greatly reduced from 46.6 wt% to 2.8 wt% after acid treatment (Table S1). Though some Ni nanoparticles can still be observed, they are sparsely distributed. In contrast, the HAADF-STEM image (Fig. 3d) reveals that numerous atomic metal sites are well dispersed on graphene layers.

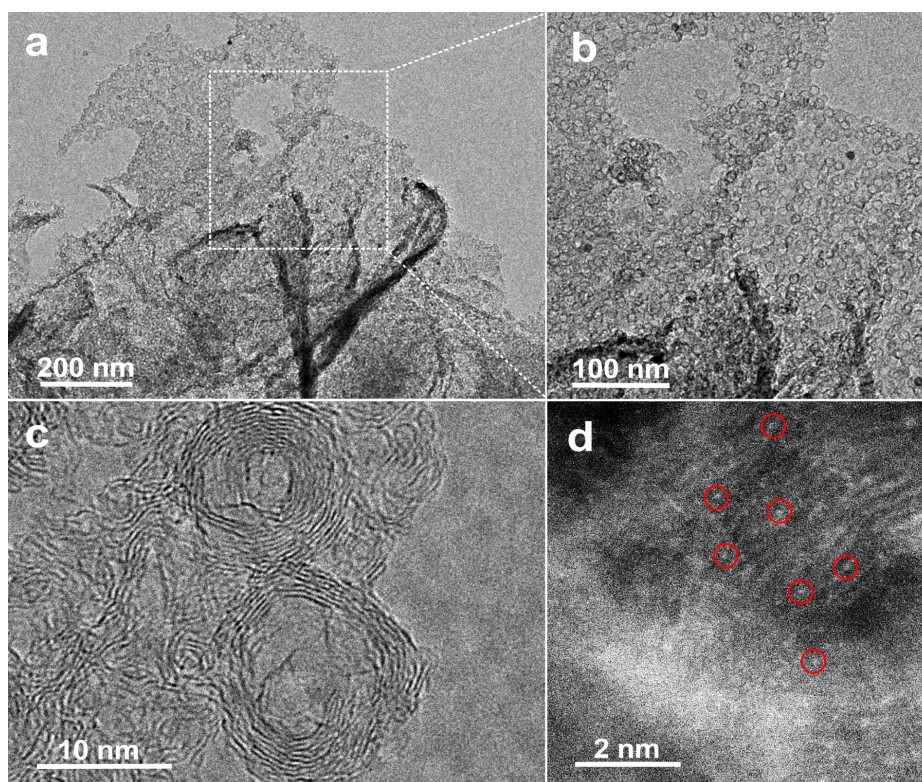


**Fig. 3.** a-c) TEM and d) HAADF-STEM image of Ni-NG-acid (atomic Ni are marked with red circles).

The XRD results (Fig. 4a) show that the (111), (200) and (220) diffraction peaks of metallic Ni phase (PDF #04-0850) in Ni-NG-acid are almost completely diminished, consistent with the much-reduced Ni content from Ni-NG after acid leaching. A broad peak around  $26^\circ$  is ascribed to (002) diffraction of graphene layers. For comparison, the morphology and structure of samples (denoted as Ni NPs@NG) derived from Ni-MOF were also characterized by SEM (Fig. S7), TEM and HRTEM (Fig. S8). In contrast, after acid treatment, extensive Ni nanoparticles of around 20-50 nm are still evenly dispersed in the sample (denoted as Ni NPs@NG-acid). The nanoparticles are also encapsulated by graphene layers and hollow graphene shells are barely found in Ni NPs@NG-acid. The measured Ni content in Ni NPs@NG-acid is as high as 52 wt% (Table S1). Such results indicate that the type of organic ligands and their interaction with the metal cations play an important role in the aggregation property of metal in MOF-derived catalyst during annealing process. The XRD patterns of Ni NPs@NG and Ni NPs@NG-acid in Fig. S9 show similar peak intensities, indicating negligible change in the Ni content, consistent with the TEM observation. Due to the presence of  $\text{-NH}_2$  functional group in  $\text{NH}_2\text{-BDC}$  ligand, the N/C ratio of Ni-NG-acid was measured to be

0.029 which is more than twice as much as that of Ni NPs@NG-acid (Table S2). The BET specific surface area of Ni-NG-acid was measured to be 651 m<sup>2</sup> g<sup>-1</sup> (Table S3), which is much larger than that of Ni NPs@NG-acid (145 m<sup>2</sup> g<sup>-1</sup>) due to the creation of hollow carbon shell structures after removing Ni NPs. Since the surface area is mainly contributed by the graphene shells, the specific surface area by excluding Ni content was calculated as well. In this instance, the specific surface area of graphene and the adsorption average pore diameter in Ni NPs@NG-acid (301 m<sup>2</sup> g<sup>-1</sup> and 5.7 nm, respectively) are still much lower than that in Ni-NG-acid (667 m<sup>2</sup> g<sup>-1</sup> and 13.3 nm), indicating a more porous nature of graphene in the latter catalyst after acid treatment. The Raman spectra in Fig. 4b presents the characteristic features of graphene. Two peaks at around 1350 and 1580 cm<sup>-1</sup>, which are respectively assigned to the D-band and G-band, are observed in all three samples. The -NH<sub>2</sub> containing ligands in the MOF precursor is evidenced to induce higher disorder in graphene layers after annealing and acid treatment based on higher intensity ratio of D- and G-band ( $I_D/I_G$ ) in Ni-NG-acid ( $I_D/I_G$  = 0.96) than Ni NPs@NG-acid ( $I_D/I_G$  = 0.52). The higher disorder and more defects of graphene structure in Ni-NG-acid are attributed to extra nitrogen doping on graphene shells from the NH<sub>2</sub>-containing ligand of NH<sub>2</sub>-Ni-MOF and selective C-N bond cleavages attributed to adjacent Ni sites[54]. To further investigate the chemical states and bonding information, X-ray photoelectron spectroscopy (XPS) analysis was carried out. As shown in Fig. 4c, the Ni 2p<sub>3/2</sub> peak at 853.1 eV corresponding to metallic Ni<sup>0</sup> in Ni-NG is almost missing in Ni-NG-acid due to the leaching of Ni NPs. On the other hand, the dominant peak located between the Ni<sup>0</sup> and Ni<sup>2+</sup> (~856 eV from nickel (II) phthalocyanine (NiPc)) peaks indicates the presence of low-valence Ni species on the surface which is stable against acid leaching. Though concentration measurement by XPS (Table S4) is semi-quantitative, it is reasonable to find that the surface atomic concentration of both Ni-NG and Ni-NG-acid is one order of magnitude lower than the bulk concentration determined by ICP-OES (Table S1) due to the encapsulation and embedment of Ni inside or within graphene layers. In contrast, the Ni 2p spectrum of Ni NPs@NG-acid is dominated by Ni<sup>0</sup> signal (Fig. S10). The N 1s XPS spectra (Fig. 4d) were deconvoluted into four peaks of pyridinic N (398.7 eV), Ni-N (399.6 eV),



pyrrolic N (401.1 eV) and graphitic N (402.2 eV). As expected, the Ni-N peak is more abundant in Ni-NG-acid than Ni NPs@NG-acid, thus facilitating the formation of single atom Ni catalyst stabilized by the N species (Table S4). The total N content measured by XPS is also consistent with EA (Table S2) and Raman (Fig. 4b) results.

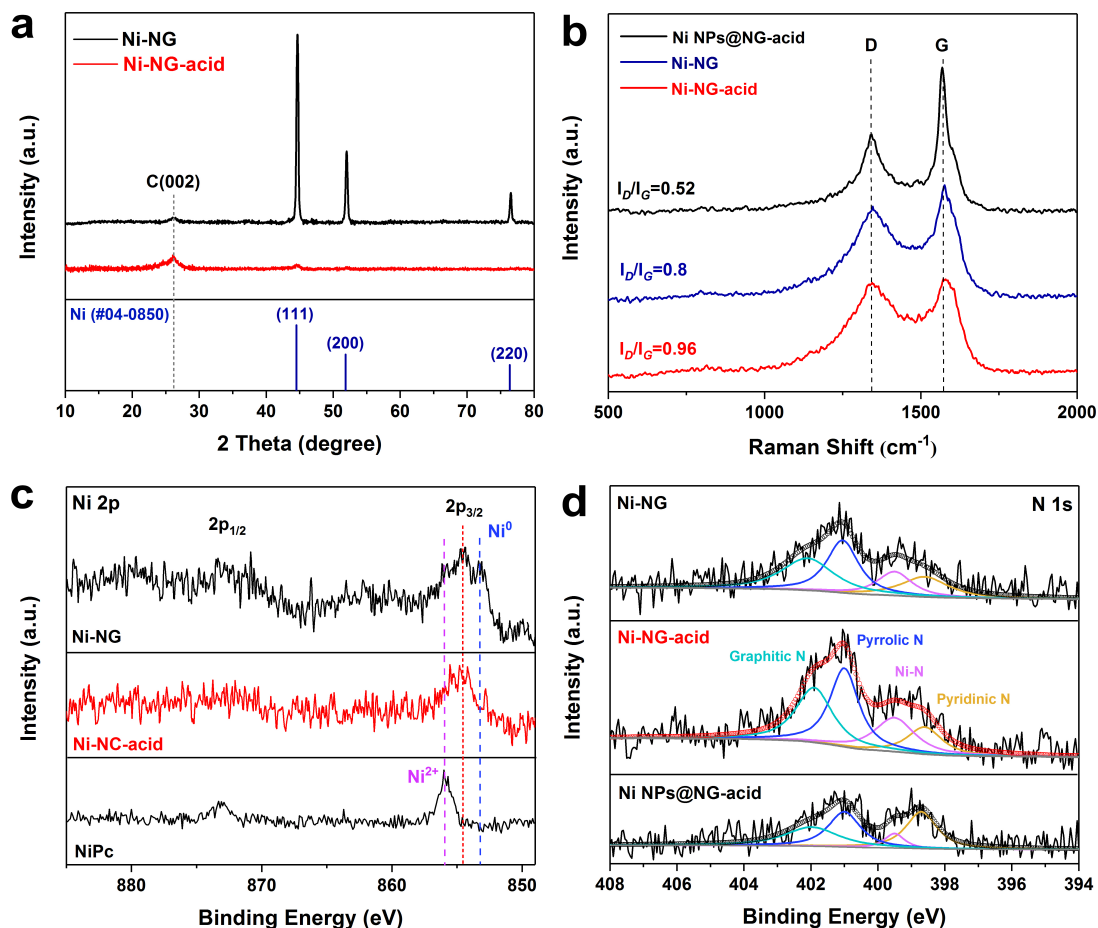


**Fig. 4.** a) XRD patterns of Ni-NG and Ni-NG-acid, b) Raman spectra of Ni NPs@NG-acid, Ni-NG and Ni-NG-acid, c) Ni 2p XPS spectra of Ni-NG, Ni-NG-acid and NiPc, d) N 1s XPS spectra of Ni-NG, Ni-NG-acid and Ni NPs@NG-acid.

The above microscopic characterization and spectroscopic analysis indicate that the Ni<sup>2+</sup> in both of Ni-MOF and NH<sub>2</sub>-Ni-MOF was reduced to Ni<sup>0</sup> crystallites by the reducing gas released from decomposed organic ligands and aggregated as Ni NPs with the size less than 10 nm at high temperature. The obtained Ni NP could subsequently serve as the catalyst seed to not only promote the decomposition of MOF precursors but also catalyze the formation of multilayer nitrogen-doped graphene shells by using gaseous carbon and nitrogen sources from decomposed organic ligands. As the “floating” particle surrounded by gaseous carbon source, the surface of spherical Ni

NPs was deposited by carbon atoms from the vapor and carbon would precipitate as a graphene shell layer during cooling process. Similar to the growth mechanism of multiwalled nanotubes (MWNTs) over Ni particles in chemical vapor deposition (CVD) method, as the particle size is reduced, multilayer graphene could be more favorable to grow on the surface of Ni NPs because of the increasing strain in all directions on the particle[55]. Since the depression of melting point depends on the surface-to-volume ratio, which is reversely proportional to the system size, the Ni still existed as a movable liquid phase during the initial stage of graphene growth. In addition, with extra N doping, the C-N cleavage could be selectively generated by the catalyzation of adjacent Ni sites on graphene layers, leading to numerous pin holes for movable Ni NPs to penetrate though the shell and aggregate to form a larger Ni particle[54]. Since the lack of remaining carbon atoms in the vapor at the later stage of graphene growth, the large Ni particle couldn't be completely sealed by graphene shell but was easily leach out by 0.5 M H<sub>2</sub>SO<sub>4</sub>, leaving only Ni-N<sub>x</sub> sites on spherical multilayer graphene shells in Ni-NG-acid. However, the multilayer graphene could protect the Ni NPs very well with not too much C-N cleavage due to less N doping and Ni NPs would be encapsulated in graphene shells.

Electrochemical CO<sub>2</sub> reduction tests were conducted in a gas-tight three electrode H-type cell with two compartments separated by Nafion-117 proton exchange membrane shown in Fig. S11. All potentials reported in this work are with reference to RHE scale. Fig. 5a shows the linear sweep voltammetry (LSV) results in 0.5 M KHCO<sub>3</sub> solution saturated with Ar or CO<sub>2</sub> gas under applied potentials in the range of 0 to -1.2 V. The gas and liquid products were analyzed by gas chromatography (GC) and <sup>1</sup>H NMR spectroscopy (Fig. S12), respectively. No liquid products but only CO and H<sub>2</sub> were detected at potentials in the range of -0.6 to -1.2 V in CO<sub>2</sub>-saturated electrolyte solution (pH = 7.2). Fig. 5b shows the influence of CO Faradaic efficiency (FE<sub>CO</sub>) by the applied potentials. Similar to other Ni nanoparticle-based catalysts [29-32, 34, 38, 39, 43, 44, 56, 57], the FE<sub>CO</sub> of Ni-NG and Ni NPs@NG-acid follows the volcano-shaped trend with increasing potential and highest FE<sub>CO</sub> less than 80%. Remarkably, Ni-NG-acid displays a rather constant FE<sub>CO</sub> of around 95-97% between -0.7 and -1.1

V, indicating excellent selectivity to CO over a wide potential range. Even at a lower (-0.6 V) or a higher (-1.2 V) potential, the  $FE_{CO}$  can still reach around 90%. The  $FE_{CO}$  for Ni-NG-acid shows superior potential-insensitive property which is speculated as a result of the easier formation of  $*COOH$  intermediate compared to  $*H$  over a large range of potentials where  $CO_2$  reduction becomes a dominating reaction. The total current density and partial current density for CO of all catalysts increase with the rising potential from -0.6 to -1.2 V (Fig. 5c,d). At potential of -0.9 V, Ni-NG-acid obtained a high CO partial current density as  $27.2 \text{ mA cm}^{-2}$  with the maximum  $FE_{CO}$  of 97%. Correspondingly, high TOFs values were obtained (Fig. 5e). For example, the TOF was calculated to be as high as  $4362 \text{ h}^{-1}$  at -1.2 V on the basis of total Ni content present in Ni-NG-acid. A lower Tafel slope in the low overpotential range indicates a faster kinetics for CO formation. In Fig. 5f, Ni-NG-acid displays a lower Tafel slope of  $121 \text{ mV dec}^{-1}$  compared with Ni NPs@NG-acid, indicating easier CO formation for Ni-NG-acid. Based on Butler-Volmer equation and Tafel equation, if there is one electron transferred in the reaction rate-determining step (RDS) and no electron transferred before RDS, the Tafel slope for overall reaction is calculated to be  $118 \text{ mV dec}^{-1}$ . All the Tafel slopes are close to the theoretical value of  $118 \text{ mV dec}^{-1}$ , which indicates the first electron-transfer to adsorb  $CO_2$  molecule is the RDS for all three catalysts [58]. Corresponding to the BET (Table S3) and electrochemical results, Ni-NG-acid was proved with higher  $CO_2$  adsorption ability compared to other catalysts (Fig. 6a), indicating that the porous structure and high surface area of Ni-NG-acid will benefit the mass transfer of the reactant and electrolyte species and also provide abundant exposed active sites for  $CO_2$  adsorption. The Nyquist plot in Fig. 6b further reveals that Ni-NG-acid has a lower interfacial charge transfer resistance than other catalysts, which facilitates a faster kinetics of  $CO_2$  reduction. Although more defects were generated on graphene layers in Ni-NG-acid according to the Raman results, more exposed Ni-N<sub>x</sub> sites on the surface made more positive influence on charge transfer. The electrochemical double-layer capacitance ( $C_{dl}$ ) was determined to compare the electrochemically active surface of the catalyst. Ni-NG-acid was found to exhibit the largest  $C_{dl}$  of  $10.65 \text{ mF cm}^{-2}$  compared to other catalysts (Fig. S13). The contact angle

of a 0.5 M  $\text{KHCO}_3$  electrolyte solution droplet on the carbon paper loaded with different catalysts was measured to explore the hydrophilic-hydrophobic interactions between the working electrode and electrolyte (Fig. S14). Ni-NG-acid loaded carbon paper was found to be more hydrophobic than others, resulting in higher affinity with nonpolar molecules, such as  $\text{CO}_2$  and less competitive HER. Based on above electrochemical measurement, Ni-NG-acid exhibits comparable or even superior electrocatalytic  $\text{CO}_2$  reduction performance with highly selective CO production and considerable TOF at low overpotentials compared with other reported Ni SACs and carbon-supported Ni NPs catalysts (Table S5).

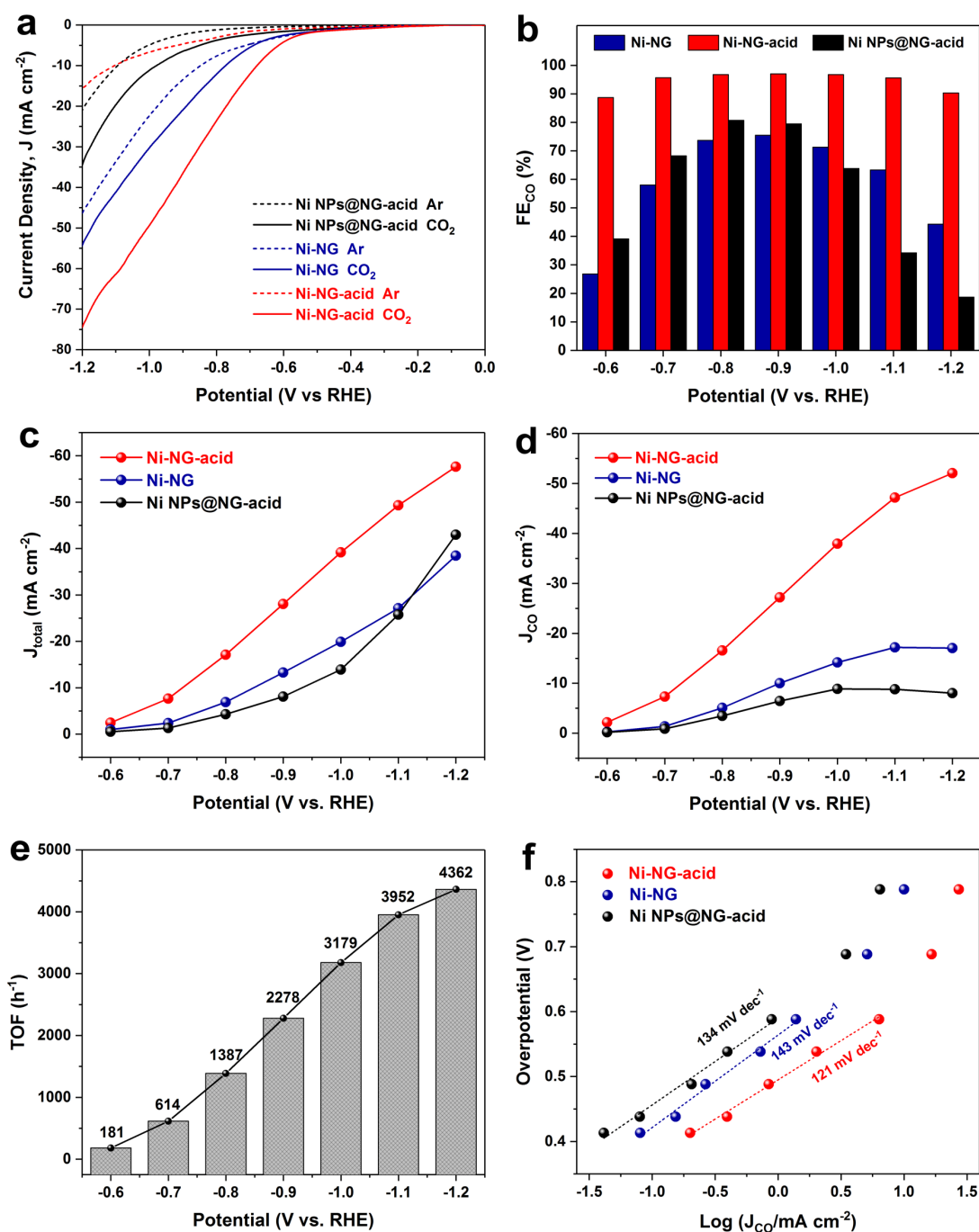


**Fig. 5.** a) The LSV curves tested in Ar-saturated (dashed line) or  $\text{CO}_2$ -saturated (solid line) 0.5 M  $\text{KHCO}_3$  electrolyte at a scan rate of  $10 \text{ mV s}^{-1}$ , b)  $\text{FE}_{\text{CO}}$ , c) total, d) partial current density plots of Ni-NG, Ni-NG-acid and Ni NPs@NG-acid at various potentials, e) TOFs for CO production of Ni-NG-acid at various potentials, f) Tafel plot of the CO partial current density for Ni-NG, Ni-NG-acid and Ni NPs@NG-acid at various potentials.

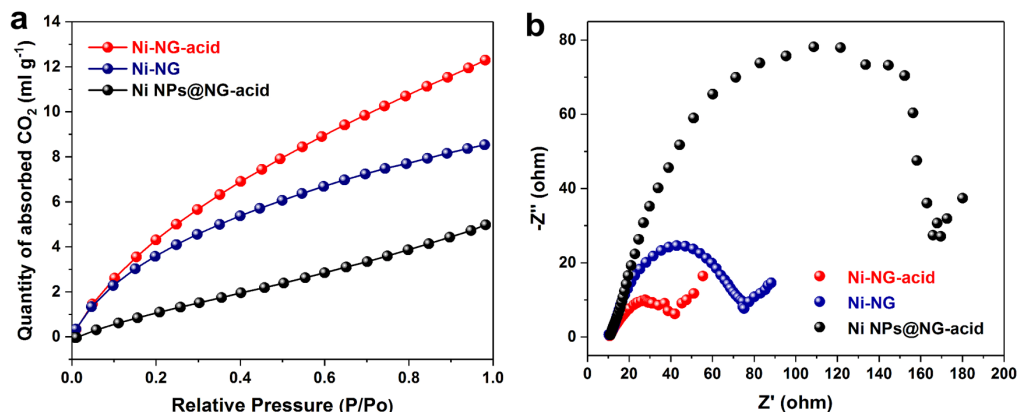


**Fig. 6.** a) CO<sub>2</sub> adsorption isotherms and b) Nyquist plots (recorded at 0.8 V vs. RHE) for Ni-NG-acid, Ni-NG and Ni NPs@NG-acid.

The effect of annealing temperature on the property and electrochemical CO<sub>2</sub> reduction performance of catalysts was investigated with the temperature varied from 700 to 1100 °C followed by the same acid treatment in 0.5 M H<sub>2</sub>SO<sub>4</sub>. The as-synthesized products are denoted as Ni-NG-X-acid (X = 700, 800, 900 and 1100). The TEM images of various samples in Fig. S15 indicate that lower temperatures (700 and 800 °C) result in higher amount of Ni NPs (~10 nm) encapsulated in graphene shells that couldn't be leached out by acid treatment. Based on more specific spectroscopic analysis, the following findings about the temperature effect on Ni-NG-X-acid samples were discussed. First of all, the XRD (Fig. S16a) result of various Ni-NG-X-acid samples exhibits that the crystallinity of graphene layers increases with higher annealing temperature where the intensity of the diffraction peak at 26° apparently rises. Second, both of the percentage of surface N (Table S6) from XPS results (Fig. S16b-d) and the bulk N measured by CHN analyzer (Fig. S17) continuously decrease with increasing annealing temperature. This perhaps due to the removal of less graphitized carbon species and unstable impurities from the decomposition of MOF precursors. Third, the Ni-NG-X-acid samples exhibit larger BET specific surface area with increasing annealing temperature from 700 to 1000 °C as a result of more exposed graphene structure after acid treatment. The surface area of Ni-NG-acid with annealing temperature of 1000 °C was found as the largest among all Ni-NG-X-acid samples in Table S3. However, the surface area dramatically dropped from 651.2 to 389 m<sup>2</sup> g<sup>-1</sup>

when the temperature was raised from 1000 to 1100 °C. This finding can be attributed to the carbon densification and sintering caused by extremely high annealing temperature, which was observed by TEM in Fig. S15g. The BET specific area based on the weight excluding Ni content was calculated as well. The Ni-NG-acid possesses the largest specific surface area on the basis of similar weight of graphene structure, which may offer more exposed catalytic sites to electrolyte. Last but not least, the ICP-OES result of various Ni-NG-X-acid samples shows consistent findings about the Ni content with TEM results. According to Table S1, the Ni content of Ni-NG-1100-acid has dropped to 1.0 wt%, much lower than samples annealed at lower temperatures. This result can be attributed to the removal of more unsealed large Ni particles by acid treatment, leading to a larger amount of hollow graphene shells in Fig. S15. Based on the similar growth mechanism of multilayer graphene on Ni surfaces in CVD method, the graphene stability sensitively depend on the growth temperature[59]. In the temperature range of 650-900 °C, graphene can even start nucleation before cooling process. With an earlier growth process and relatively more stable graphene layers produced at 700 °C, most of the Ni core with low mobility at lower temperature could be encapsulated by graphene shell and numerous Ni-graphene core-shell structure were observed in Ni-NG-700 before acid treatment. As the temperature increased, the graphene layers just formed on the Ni surface are metastable with lots of C-N cleavages, which allowed the liquid phase Ni at higher temperature to penetrate the shell and aggregate to a larger Ni particle without perfect wrapping by graphene layers. From the above findings and discussion, adjusting the annealing temperature can be considered an effective method to influence the carbonization of organic ligands and Ni aggregation for tunable size and distribution of Ni NPs. The electrochemical performances of various Ni-NG-X-acid samples are shown in Fig. 7a,b. According to the  $FE_{CO}$  and CO partial current density plots, 1000 °C has been found the optimal annealing temperature for efficient and highly selective electrochemical CO<sub>2</sub> reduction to CO. Based on the properties these catalysts, it is speculated that the better conductivity of graphene layers, more atomic Ni coordinated with N, i.e., Ni-N<sub>x</sub> moiety,

and larger surface area should be collectively responsible for the excellent performance of Ni-NG-acid among all Ni-NG-X-acid samples.

Conducting appropriate acid treatment was regarded as another effective way to control the existing form of Ni. Based on the TEM result (in Fig. 3b) and XRD pattern (in Fig. 4a) of Ni-NG-acid, very few Ni NPs inside graphene shells are still present after 0.5 M H<sub>2</sub>SO<sub>4</sub> treatment. To further elucidate the effective catalytic sites of Ni-NG-acid, we attempt to remove all remaining Ni NPs by applying severer acid treatment: 2 M H<sub>2</sub>SO<sub>4</sub> (Ni-NG-2M acid, see the experimental section) and even more violent acid leaching procedure (Ni-NG-val acid, see the experimental section). The TEM and HRTEM images of Ni-NG-2M acid and Ni-NG-val acid in Fig. S18 show that even under such conditions, the Ni NPs still exist, indicating that these Ni NPs are well isolated by the shell of graphene layers. Since they are not reachable by both H<sub>2</sub>SO<sub>4</sub> and HCl, the chance of them being contacted by the electrolytes during CO<sub>2</sub> reduction is also low and the catalytic activity should mainly stem from the single Ni site. The electrocatalytic performance of Ni-NG-2M acid and Ni-NG-val acid was also evaluated in Fig. 7c,d. The FE<sub>CO</sub> values of Ni-NG-2M acid is slighter lower than those of Ni-NG-acid at various potential. However, the current density has dropped significantly. For example, the CO partial current density is 16.6 mA cm<sup>-2</sup> at -0.9 V which is 39% lower than that of Ni-NG-acid. In the case of Ni-NG-val acid, both of the FE<sub>CO</sub> and current density are severely affected. The worse CO selectivity and electrochemical properties should be due to the damage of Ni-N<sub>x</sub> active sites under such harsh leaching condition, indicating that Ni-N<sub>x</sub> sites embedded on graphene layers play a more important role in catalyzing CO<sub>2</sub> reduction than remained Ni cores.



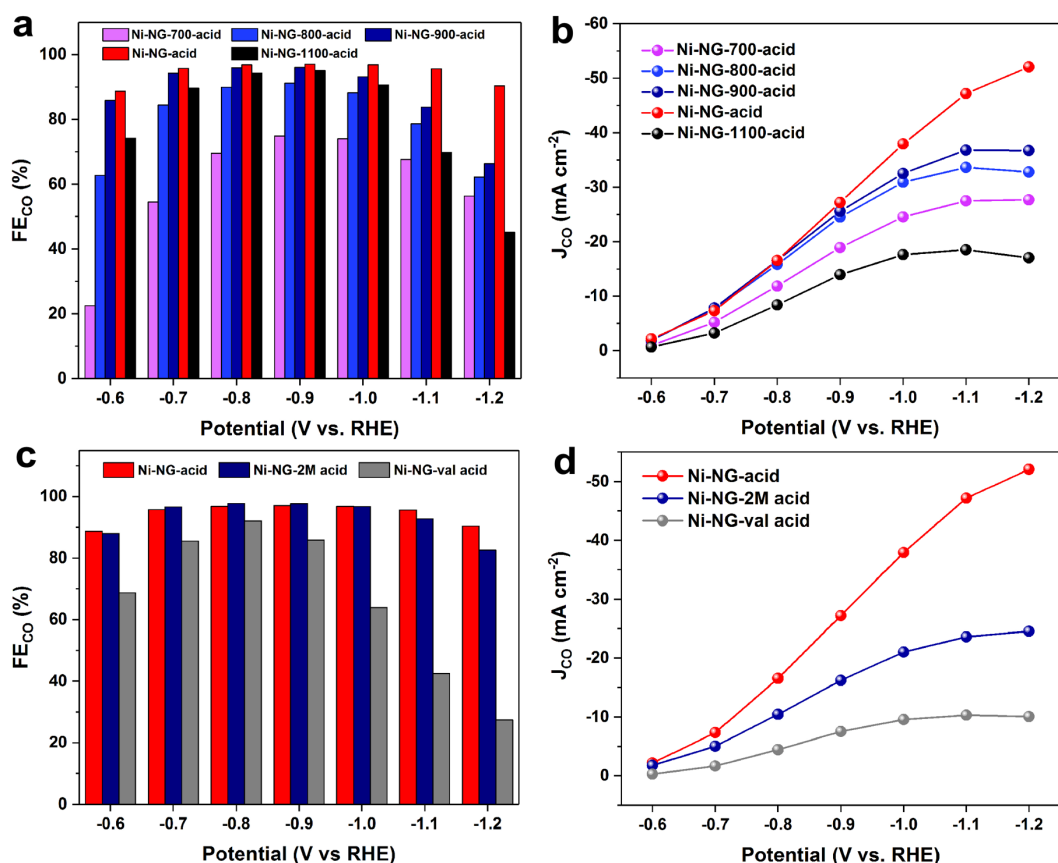


**Fig. 7.** a) FE<sub>CO</sub> and b) partial current density of various Ni-NG-X-acid catalysts at different potentials (Ni-NG-1000-acid is denoted as Ni-NG-acid), c) FE<sub>CO</sub> and d) CO partial current density of catalysts with varying degrees of acid treatments at different potentials.

#### 4. Conclusion

In summary, we report a facile synthesis method for Ni-N<sub>x</sub> single sites embedded in nitrogen-doped multilayer graphene as the efficient electrocatalyst for CO<sub>2</sub> reduction with high CO selectivity over a wide range of potentials. Control study has shown that the NH<sub>2</sub>-containing building block of the MOF is responsible for the formation of Ni-N<sub>x</sub> active sites on graphene shells, achieving efficient electrocatalytic CO<sub>2</sub> reduction with FE<sub>CO</sub> of 95-97% over a wide potential range from -0.7 to -1.1 V and considerable partial current density. According to the discussion on material characterization, the importation of -NH<sub>2</sub> groups in MOF precursor can not only lead in excessive nitrogen source but also make a significant influence on chemical coordination environment of metal. The nitrogen in NH<sub>2</sub>-containing organic ligands can be chemically coordinated with the metal cations in the MOF precursor, promoting the generation of abundant Ni-

N<sub>x</sub> moieties on graphene layers after annealing. In addition, the presence of -NH<sub>2</sub> was also demonstrated the ability of influencing the formation C-N cleavages during the later annealing process by the observation from TEM, resulting in the liquid phase Ni core penetrating through the graphene shell and further aggregation. For the same MOF precursor, the synergistic effect of the annealing process under appropriate temperature and acid treatment in mild condition is able to collectively control the carbonization and removal of metal particles, leading to optimal surface environment with abundant catalytic Ni-N<sub>x</sub> single sites and efficient electron transfer ability. With sufficient discussion on the chemical environment in MOF precursor and the graphene formation on Ni surface on the nano level, we expect the mentioned strategy in this work will provide us with new insight on the synthesis of M-N-C type catalysts by annealing the NH<sub>2</sub>-containing ligands in various N-rich MOFs for CO<sub>2</sub> reduction or other applications.

### **Conflicts of interest**

There are no conflicts to declare.

### **Acknowledgements**

This work is supported by Nanyang Technological University, Singapore (Grant RG116/16) and by the Singapore National Research Foundation under its Campus for Research Excellence and Technological Enterprise (CREATE) program through the Cambridge Center for Advanced Research and Education in Singapore (CARES) Cambridge Center for Carbon Reduction in Chemical Technology (C4T) and through CARES and the Berkeley Educational Alliance for Research in Singapore (BEARS) eCO2P program. We also would like to express our gratitude to Neil Young and Lan Griffiths who helped us operate JEOL ARM-200F in David Cockayne Centre for Electron Microscopy, Oxford University.

### **References**

- [1] B.P. Sullivan, K. Krist, H. Guard, *Electrochemical and Electrocatalytic Reactions of Carbon Dioxide*, Elsevier, New York, 2012.

- [2] D.D. Zhu, J.L. Liu, S.Z. Qiao, Recent advances in inorganic heterogeneous electrocatalysts for reduction of carbon dioxide, *Adv. Mater.* 28 (2016) 3423-3452.
- [3] Y. Wu, Q. Zhu, B. Zhu, Decoupling analysis of world economic growth and CO<sub>2</sub> emissions: A study comparing developed and developing countries, *J. Clean. Prod.* 190 (2018) 94-103.
- [4] Z.L. Wang, C. Li, Y. Yamauchi, Nanostructured nonprecious metal catalysts for electrochemical reduction of carbon dioxide, *Nano Today* 11 (2016) 373-391.
- [5] B. Khezri, A.C. Fisher, M. Pumera, CO<sub>2</sub> reduction: the quest for electrocatalytic materials, *J. Mater. Chem. A* 5 (2017) 8230-8246.
- [6] C. Steinlechner, A.F. Roesel, E. Oberem, A. Pöpcke, N. Rockstroh, F. Gloaguen, S. Lochbrunner, R. Ludwig, A. Spannenberg, H. Junge, R. Francke, M. Beller, Selective earth-abundant system for CO<sub>2</sub> reduction: Comparing photo- and electrocatalytic processes, *ACS Catal.* 9 (2019) 2091-2100.
- [7] T. Ma, Q. Fan, H. Tao, Z. Han, M. Jia, Y. Gao, W. Ma, Z. Sun, Heterogeneous electrochemical CO<sub>2</sub> reduction using nonmetallic carbon-based catalysts: current status and future challenges, *Nanotechnology* 28 (2017) 472001.
- [8] F. Li, D.R. MacFarlane, J. Zhang, Recent advances in the nanoengineering of electrocatalysts for CO<sub>2</sub> reduction, *Nanoscale* 10 (2018) 6235-6260.
- [9] Q. Lu, F. Jiao, Electrochemical CO<sub>2</sub> reduction: Electrocatalyst, reaction mechanism, and process engineering, *Nano Energy* 29 (2016) 439-456.
- [10] X. Duan, J. Xu, Z. Wei, J. Ma, S. Guo, S. Wang, H. Liu, S. Dou, Metal-free carbon materials for CO<sub>2</sub> electrochemical reduction, *Adv. Mater.* 29 (2017) 1701784.
- [11] A.J. Martín, G.O. Larrazábal, J. Pérez-Ramírez, Towards sustainable fuels and chemicals through the electrochemical reduction of CO<sub>2</sub>: lessons from water electrolysis, *Green Chem.* 17 (2015) 5114-5130.
- [12] D. Kim, C. Xie, N. Becknell, Y. Yu, M. Karamad, K. Chan, E.J. Crumlin, J.K. Nørskov, P. Yang, Electrochemical activation of CO<sub>2</sub> through atomic ordering transformations of AuCu nanoparticles, *J. Am. Chem. Soc.* 139 (2017) 8329-8336.
- [13] Z. Cao, S.B. Zacate, X. Sun, J. Liu, E.M. Hale, W.P. Carson, S.B. Tyndall, J. Xu, X. Liu, X. Liu, C. Song, J.H. Luo, M.J. Cheng, X. Wen, W. Liu, Tuning gold

nanoparticles with chelating ligands for highly efficient electrocatalytic CO<sub>2</sub> reduction, *Angew. Chem. Int. Ed.* 57 (2018) 12675-12679.

[14] D. Gao, H. Zhou, F. Cai, J. Wang, G. Wang, X. Bao, Pd-containing nanostructures for electrochemical CO<sub>2</sub> reduction reaction, *ACS Catal.* 8 (2018) 1510-1519.

[15] Z. Han, C. Choi, H. Tao, Q. Fan, Y. Gao, S. Liu, A.W. Robertson, S. Hong, Y. Jung, Z. Sun, Tuning the Pd-catalyzed electroreduction of CO<sub>2</sub> to CO with reduced overpotential, *Catal. Sci. Technol.* 8 (2018) 3894-3900.

[16] X. Peng, S.G. Karakalos, W.E. Mustain, Preferentially oriented Ag nanocrystals with extremely high activity and faradaic efficiency for CO<sub>2</sub> electrochemical reduction to CO, *ACS Appl. Mater. Interfaces* 10 (2018) 1734-1742.

[17] S. Zhao, R. Jin, R. Jin, Opportunities and challenges in CO<sub>2</sub> reduction by gold- and silver-based electrocatalysts: From bulk metals to nanoparticles and atomically precise nanoclusters, *ACS Energy Lett.* 3 (2018) 452-462.

[18] S. Zhu, Q. Wang, X. Qin, M. Gu, R. Tao, B.P. Lee, L. Zhang, Y. Yao, T. Li, M. Shao, Tuning structural and compositional effects in Pd-Au nanowires for highly selective and active CO<sub>2</sub> electrochemical reduction reaction, *Adv. Energy Mater.* 8 (2018) 1802238.

[19] K. Liu, M. Ma, L. Wu, M. Valenti, D. Cardenas-Morcoso, J.P. Hofmann, J. Bisquert, S. Gimenez, W.A. Smith, Electronic effects determine the selectivity of planar Au-Cu bimetallic thin films for electrochemical CO<sub>2</sub> reduction, *ACS Appl. Mater. Interfaces* 11 (2019) 16546-16555.

[20] S. Mezzavilla, S. Horch, I.E.L. Stephens, B. Seger, I. Chorkendorff, Structure sensitivity in the electrocatalytic reduction of CO<sub>2</sub> with gold catalysts, *Angew. Chem. Int. Ed.* 58 (2019) 3774-3778.

[21] Z. Sun, T. Ma, H. Tao, Q. Fan, B. Han, Fundamentals and challenges of electrochemical CO<sub>2</sub> reduction using two-dimensional materials, *Chem* 3 (2017) 560-587.

[22] G. Liu, Y. Sheng, J.W. Ager, M. Kraft, R. Xu, Research advances towards large-scale solar hydrogen production from water, *EnergyChem* 1 (2019) 100014.

[23] S. Lin, C.S. Diercks, Y. Zhang, N. Kornienko, E.M. Nichols, Y. Zhao, A.R. Paris,

d. Kim, P. Yang, O.M. Yaghi, C.J. Chang, Cobalt porphyrins COF for CO<sub>2</sub> reduction in water, *Science* 349 (2015) 1208-1213.

[24] I. Azcarate, C. Costentin, M. Robert, J.M. Saveant, Through-space charge interaction substituent effects in molecular catalysis leading to the design of the most efficient catalyst of CO<sub>2</sub>-to-CO electrochemical conversion, *J. Am. Chem. Soc.* 138 (2016) 16639-16644.

[25] B. Rungtaweeveranit, J. Baek, J.R. Araujo, B.S. Archanjo, K.M. Choi, O.M. Yaghi, G.A. Somorjai, Copper nanocrystals encapsulated in Zr-based metal-organic frameworks for highly selective CO<sub>2</sub> hydrogenation to methanol, *Nano Lett.* 16 (2016) 7645-7649.

[26] Eva M. Nichols, J.S. Derrick, S.K. Nistanaki, P.T. Smith, C.J. Chang, Positional effects of second-sphere amide pendants on electrochemical CO<sub>2</sub> reduction catalyzed by iron porphyrins, *Chem. Sci.* 9 (2018) 2952-2960.

[27] S. Nitopi, E. Bertheussen, S.B. Scott, X. Liu, A.K. Engstfeld, S. Horch, B. Seger, I.E.L. Stephens, K. Chan, C. Hahn, J.K. Nørskov, T.F. Jaramillo, I. Chorkendorff, Progress and perspectives of electrochemical CO<sub>2</sub> reduction on copper in aqueous electrolyte, *Chem. Rev.* 119 (2019) 7610-7672.

[28] Y. Chen, S. Ji, Y. Wang, J. Dong, W. Chen, Z. Li, R. Shen, L. Zheng, Z. Zhuang, D. Wang, Y. Li, Isolated single iron atoms anchored on N-doped porous carbon as an efficient electrocatalyst for the oxygen reduction reaction, *Angew. Chem. Int. Ed.* 56 (2017) 6937-6941.

[29] C. Zhao, X. Dai, T. Yao, W. Chen, X. Wang, J. Wang, J. Yang, S. Wei, Y. Wu, Y. Li, Ionic exchange of metal-organic frameworks to access single nickel sites for efficient electroreduction of CO<sub>2</sub>, *J. Am. Chem. Soc.* 139 (2017) 8078-8081.

[30] Y. Cheng, S. Zhao, B. Johannessen, J.P. Veder, M. Saunders, M.R. Rowles, M. Cheng, C. Liu, M.F. Chisholm, R. De Marco, H.M. Cheng, S.Z. Yang, S.P. Jiang, Atomically dispersed transition metals on carbon nanotubes with ultrahigh loading for selective electrochemical carbon dioxide reduction, *Adv. Mater.* 30 (2018) 1706287.

[31] K. Jiang, S. Siahrostami, T. Zheng, Y. Hu, S. Hwang, E. Stavitski, Y. Peng, J. Dynes, M. Gangisetty, D. Su, K. Attenkofer, H. Wang, Isolated Ni single atoms in graphene

nanosheets for high-performance CO<sub>2</sub> reduction, *Energy Environ. Sci.* 11 (2018) 893-903.

[32] H.B. Yang, S.F. Hung, S. Liu, K. Yuan, S. Miao, L. Zhang, X. Huang, H.Y. Wang, W. Cai, R. Chen, J. Gao, X. Yang, W. Chen, Y. Huang, H.M. Chen, C.M. Li, T. Zhang, B. Liu, Atomically dispersed Ni(i) as the active site for electrochemical CO<sub>2</sub> reduction, *Nat. Energy* 3 (2018) 140-147.

[33] M. Jia, Q. Fan, S. Liu, J. Qiu, Z. Sun, Single-atom catalysis for electrochemical CO<sub>2</sub> reduction, *Curr. Opin. Green Sustain. Chem.* 16 (2019) 1-6.

[34] T. Zheng, K. Jiang, N. Ta, Y. Hu, J. Zeng, J. Liu, H. Wang, Large-scale and highly selective CO<sub>2</sub> electrocatalytic reduction on nickel single-atom catalyst, *Joule* 3 (2019) 265-278.

[35] Y. Lu, H. Wang, P. Yu, Y. Yuan, R. Shahbazian-Yassar, Y. Sheng, S. Wu, W. Tu, G. Liu, M. Kraft, R. Xu, Isolated Ni single atoms in nitrogen doped ultrathin porous carbon templated from porous g-C<sub>3</sub>N<sub>4</sub> for high-performance CO<sub>2</sub> reduction, *Nano Energy* (2020) in press.

[36] X.-F. Yang, A. Wang, B. Qiao, J. Li, J. Liu, T. Zhang, Single-atom catalysts: A new frontier in heterogeneous catalysis, *Acc. Chem. Res.* 46 (2013) 1740-1748.

[37] J. Guo, J. Huo, Y. Liu, W. Wu, Y. Wang, M. Wu, H. Liu, G. Wang, Nitrogen-doped porous carbon supported nonprecious metal single-atom electrocatalysts: from synthesis to application, *Small Methods* 3 (2019) 1900159.

[38] W. Ju, A. Bagger, G.P. Hao, A.S. Varela, I. Sinev, V. Bon, B. Roldan Cuenya, S. Kaskel, J. Rossmeisl, P. Strasser, Understanding activity and selectivity of metal-nitrogen-doped carbon catalysts for electrochemical reduction of CO<sub>2</sub>, *Nat. Commun.* 8 (2017) 944.

[39] W. Bi, X. Li, R. You, M. Chen, R. Yuan, W. Huang, X. Wu, W. Chu, C. Wu, Y. Xie, Surface immobilization of transition metal ions on nitrogen-doped graphene realizing high-efficient and selective CO<sub>2</sub> reduction, *Adv. Mater.* 30 (2018) 1706617.

[40] N. Leonard, W. Ju, I. Sinev, J. Steinberg, F. Luo, A.S. Varela, B. Roldan Cuenya, P. Strasser, The chemical identity, state and structure of catalytically active centers during the electrochemical CO<sub>2</sub> reduction on porous Fe-nitrogen-carbon (Fe-N-C)

materials, *Chem. Sci.* 9 (2018) 5064-5073.

[41] A.S. Varela, W. Ju, P. Strasser, Molecular nitrogen-carbon catalysts, solid metal organic framework catalysts, and solid metal/nitrogen-doped carbon (MNC) catalysts for the electrochemical CO<sub>2</sub> reduction, *Adv. Energy Mater.* 8 (2018) 1703614.

[42] W. Ren, X. Tan, W. Yang, C. Jia, S. Xu, K. Wang, S.C. Smith, C. Zhao, Isolated diatomic Ni-Fe metal-nitrogen sites for synergistic electroreduction of CO<sub>2</sub>, *Angew. Chem. Int. Ed.* 58 (2019) 6972-6976.

[43] X. Li, W. Bi, M. Chen, Y. Sun, H. Ju, W. Yan, J. Zhu, X. Wu, W. Chu, C. Wu, Y. Xie, Exclusive Ni-N<sub>4</sub> sites realize near-unity CO selectivity for electrochemical CO<sub>2</sub> reduction, *J. Am. Chem. Soc.* 139 (2017) 14889-14892.

[44] P. Lu, Y. Yang, J. Yao, M. Wang, S. Dipazir, M. Yuan, J. Zhang, X. Wang, Z. Xie, G. Zhang, Facile synthesis of single-nickel-atomic dispersed N-doped carbon framework for efficient electrochemical CO<sub>2</sub> reduction, *Appl. Catal., B* 241 (2019) 113-119.

[45] C.-Z. Yuan, K. Liang, X.-M. Xia, Z.-K. Yang, Y.-F. Jiang, T. Zhao, C. Lin, T.-Y. Cheang, S.-L. Zhong, A.-W. Xu, Powerful CO<sub>2</sub> electroreduction performance with N-carbon doped with single Ni atoms, *Catal. Sci. Technol.* 9 (2019) 3669-3674.

[46] T. Möller, W. Ju, A. Bagger, X. Wang, F. Luo, T. Ngo Thanh, A.S. Varela, J. Rossmeisl, P. Strasser, Efficient CO<sub>2</sub> to CO electrolysis on solid Ni-N-C catalysts at industrial current densities, *Energy Environ. Sci.* 12 (2019) 640-647.

[47] M. Zhang, T.-S. Wu, S. Hong, Q. Fan, Y.-L. Soo, J. Masa, J. Qiu, Z. Sun, Efficient electrochemical reduction of CO<sub>2</sub> by Ni-N catalysts with tunable performance, *ACS Sustain. Chem. Eng.* 7 (2019) 15030-15035.

[48] Z. Liang, R. Zhao, T. Qiu, R. Zou, Q. Xu, Metal-organic framework-derived materials for electrochemical energy applications, *EnergyChem* 1 (2019) 100001.

[49] Y. Xu, W. Tu, B. Zhang, S. Yin, Y. Huang, M. Kraft, R. Xu, Nickel nanoparticles encapsulated in few-layer nitrogen-doped graphene derived from metal-organic frameworks as efficient bifunctional electrocatalysts for overall water splitting, *Adv. Mater.* 29 (2017) 1605957.

[50] P. Maniam, N. Stock, Investigation of porous Ni-based metal-organic frameworks

containing paddle-wheel type inorganic building units via high-throughput methods, *Inorg. Chem.* 50 (2011) 5085-5097.

[51] L. Asgharnejad, A. Abbasi, A. Shakeri, Ni-based metal-organic framework/GO nanocomposites as selective adsorbent for CO<sub>2</sub> over N<sub>2</sub>, *Micropor. Mesopor. Mat.* 262 (2018) 227-234.

[52] M. Athar, U. Farooq, M. Aslam, M. Salman, Adsorption of Pb(II) ions onto biomass from *Trifolium resupinatum*: equilibrium and kinetic studies, *Appl. Water Sci.* 3 (2013) 665-672.

[53] P. Larkin, *Infrared and Raman Spectroscopy: Principles and Spectral Interpretation*, Elsevier, Amsterdam, 2011.

[54] Y. He, S. Liu, C. Priest, Q. Shi, G. Wu, Atomically dispersed metal-nitrogen-carbon catalysts for fuel cells: advances in catalyst design, electrode performance, and durability improvement, *Chem. Soc. Rev.* 49 (2020) 3484-3524.

[55] S.B. Sinnott, R. Andrews, D. Qian, A.M. Rao, Z. Mao, E.C. Dickey, F. Derbyshire, Model of carbon nanotube growth through chemical vapor deposition, *Chem. Phys. Lett.* 315 (1999) 25-30.

[56] M. Jia, C. Choi, T.S. Wu, C. Ma, P. Kang, H. Tao, Q. Fan, S. Hong, S. Liu, Y.L. Soo, Y. Jung, J. Qiu, Z. Sun, Carbon-supported Ni nanoparticles for efficient CO<sub>2</sub> electroreduction, *Chem. Sci.* 9 (2018) 8775-8780.

[57] C.-Z. Yuan, H.-B. Li, Y.-F. Jiang, K. Liang, S.-J. Zhao, X.-X. Fang, L.-B. Ma, T. Zhao, C. Lin, A.-W. Xu, Tuning the activity of N-doped carbon for CO<sub>2</sub> reduction via in situ encapsulation of nickel nanoparticles into nano-hybrid carbon substrates, *J. Mater. Chem. A* 7 (2019) 6894-6900.

[58] Y.H. Fang, Z.P. Liu, Tafel kinetics of electrocatalytic reactions: From experiment to first-principles, *ACS Catal.* 4 (2014) 4364-4376.

[59] M.B. A. Dahal, Graphene-nickel interfaces: a review, *Nanoscale* 6 (2014) 2548-2562.